8th AIAA Flow Control Conference, 13-17 June 2016, Washington DC, USA
DOI:10.2514/6.2016-3177

Wavelet Analysis of Complex-Geometry Transonic Cavity Flows

D. Bacci[1] and A.J. Saddington[2]
Cranfield University, Defence Academy of the UK, Shrivenham, SN6 8LA, United Kingdom

and

D.Bray[3]
Cranfield University, Defence Academy of the UK, Shrivenham, SN6 8LA, United Kingdom

The aero-acoustic analysis of a weapon bay of an Unmanned Combat Air Vehicle (UCAV) was predicted using Computational Fluid Dynamics (CFD) methods. Along the reference geometry, consisting in the installation of the Boeing M219 modified type cavity in the Boeing UCAV1303 airframe, two additional configurations, developed modifying the leading and trailing edge geometries of the bay, were tested. Pressure signals inside the cavity were post-processed using Joint Time Frequency Analysis (JTFA) techniques, consisting in a combination of frequency domain and time-frequency domain techniques based respectively on the Fourier and wavelet transform. Results showed an intermittency nature of the modes present in the spectra as well as a continuous change, during the temporal evolution of the signal, of the dominant mode. Also were recorded, using second order wavelet spectral moments, non-linear phenomena between the main modes like phase coupling.

Nomenclature

CFL	=	Courant–Friedrichs–Lewy condition
D	=	cavity depth [m]
FFT	=	fast Fourier transform
JTFA	=	joint time-frequency analysis
L	=	cavity length [m]
OASPL	=	overall sound pressure level [dB]
PSD	=	power spectral density
SPL	=	sound pressure level [dB]
W	=	cavity width [m]
WBC	=	wavelet bi-coherence
WBS	=	wavelet bi-spectrum
C_p	=	pressure coefficient
F_s	=	sampling frequency [Hz]
F_r	=	frequency resolution [Hz]
f	=	frequency [Hz]
y^+	=	boundary layer non-dimensional height
Q	=	second invariant of the velocity gradient tensor [1/s^2]
St	=	Strouhal number ($f \cdot L/U_\infty$)
H	=	altitude [ft]
M_∞	=	Mach number in undisturbed flow
U_∞	=	free stream speed in undisturbed flow [m/s]

[1] PhD Researcher, Aeromechanical Systems Group, d.bacci@cranfield.ac.uk, AIAA member
[2] Senior Lecturer, Aeromechanical Systems Group, a.j.saddington@cranfield.ac.uk
[3] Senior Lecturer, Aeromechanical Systems Group, d.bray@cranfield.ac.uk

ρ_∞ = air density in undisturbed flow [kg/m^3]
p_∞ = air pressure in undisturbed flow [Pa]
T_∞ = air temperature in undisturbed flow [K]
ν_∞ = kinematic viscosity in undisturbed flow [m^2/s]
μ_∞ = dynamic viscosity in undisturbed flow [kg/ms]
a_∞ = sound speed in undisturbed flow [m/s]
γ = ratio of specific heats (1.4 for air)
k_∞ = turbulent kinetic energy at far-field [m^2/s^2]
ω_∞ = turbulent specific dissipation rate at far-field [1/s]
α = angle of attack [deg]
β = angle of sideslip [deg]
σ = root mean square
Mn = nth Rossiter-Heller mode
Shm_{Mn} = mth sub-harmonic of nth Rossiter-Heller mode
Hm_{Mn} = mth harmonic of nth Rossiter-Heller mode
$Sb_{Mp\pm Mq}$ = sub-mode created by the non-linear interaction in sum/difference of pth mode and qth mode

I. Introduction

THE requirement for modern aircraft to have a reduced radar-cross-section (RCS), as well as improved aerodynamic performances, has introduced the need to incorporate weapon bays in future combat aircraft designs, especially for next generation unmanned combat air vehicles (UCAV). When the bay doors are opened, the flow in the weapon bay becomes highly turbulent and unsteady, hazarding any possible jettison operation. Moreover airframe and weapon can be damaged from the intense acoustic field that is developed by the flows which can produce unsteady pressure levels of up to 170 dB at particular resonant modes. This resonance is typical of cavity flows, which have been extensively studied over the years [1]. These frequencies, at which this resonance behaviour occurs, called Rossiter modes [2], can be estimated, in compressible flow, using Heller and Bliss's semi empirical method [3]. However, both the Heller and Rossiter method were developed for rectangular cavities. Moreover these equations cannot predict the distribution of the modal amplitudes, which vary greatly depending on flow condition and cavity geometry. Previous experiments in rectangular cavities of various depths have been conducted to study the unsteady fluctuations and to understand the physics behind the phenomenon [4,5]. However, there are limitations when applying this work to aircraft bays, which have many complex features that are not captured by simple rectangular cavity geometry [6]. Limited work has been published in open literature regarding studies on cavities that are not simply rectangular and isolated from the rest of the aircraft [7,8,9,10,11] and limited work has been conducted in understanding the differences from simple geometries. To address this shortcoming it was decided to install a Boeing M-219 type-cavity in a Boeing UCAV1303 airframe and to investigate the effects of two geometrical configurations derived by common guidelines in the design of stealth aircraft, which is the adoption of serrated edges. The configuration was also provided of bay doors, which detrimental effects on the flow have already been studied and described [12]. It has been decided to analyse a full scale dimension aircraft instead to consider wind-tunnel size dimensions models like in previous studies [9,11]. Also it has been chosen to consider temporal histories equal to typical combat situation ones. In fact in these situations a full bay cycle[4] is completed in less than 4 s, to reduce the probability of detection as well as the adverse aerodynamics effect, implying that the open configuration, which is studied in this paper, is maintained for a maximum period of 2 s. Hence it is mandatory to give more attention to shorter histories and to time-frequency domain phenomena in order to correctly reproduce an in-flight situation. A longer sample, even if better from statistical and confidence points of view, suffers from the fact that represents an averaged reality that rarely is encountered in field operations.

The analysis has been conducted via numerical simulation using the Detached Eddy Simulation (DES) turbulence model, which capabilities to resolve the cavity flow problem has been already investigated and validated [9,11]. CFD data was also accompanied by a wind tunnel campaign in which the cavity geometries, installed in in a flat plate, where tested. Unsteady analysis of the data obtained from the simulation has been performed using the standard frequency domain approach coupled with a time-frequency domain analysis based on the wavelet transform. The justification resides in the fact that the assumption of statistical stationarity of the phenomenon, which is at the base of the frequency domain analysis, can produce information loss due to the fact that aerodynamic

[4] A bay cycle is a cycle where the doors start closed, then are opened till the maximum aperture and kept in that position for enough time for a safe store release, and then are closed again.

turbulence, by its very nature, is not statistically stationary and hence neither is any phenomenon deriving from it. This is also the case of cavity flows as shown in the results of Lawson & Barakos [13]. The wavelet transform is a powerful method for time-frequency analysis and its application, in non-stationary statistical data, has already showed its capability. Camussi, et al. [14] have used wavelet transform in the analysis of wall pressure fluctuations of boundary layers. Li [15] as well as Lee & Sung [16] used it to successfully identify coherent structures in turbulent shear flow while, Watanabe, et al. [17] used wavelets to decompose vorticity near the turbulent/non-turbulent interface in a turbulent jet in coherent and non-coherent structures. In the post processing of simple rectangular cavities using wavelet transform can be found the work of Wagner, et al. [18] where they used it to evidence the non-linear effect of mode switching and as starting base of their phase-averaging procedure. Kengerise, et al. [19] too based their works on wavelet to describe the mode-switching phenomenon. In this study the analysis of the effects of the modification of the cavity geometry was performed using Joint Time-Frequency Analysis techniques. JTFA is a combination of frequency domain and time-frequency domain analysis procedures especially suited for tracking both linear and non-linear phenomena typical of transonic complex configuration cavities.

II. Numerical Simulation

A. Geometry

The Boeing/AFRL 1303 model used in this research is a generic UCAV with a blended wing body (BWB) layout with an overall length of 10 m and an overall span of 16.5 m. The airframe is completed by the installation of two Boeing/M219 type weapon bays. The global layout is depicted in Figure 1. The aircraft is a transonic bomber drone for air to ground mission, capable of delivering two standard class 500lbs bombs on target.

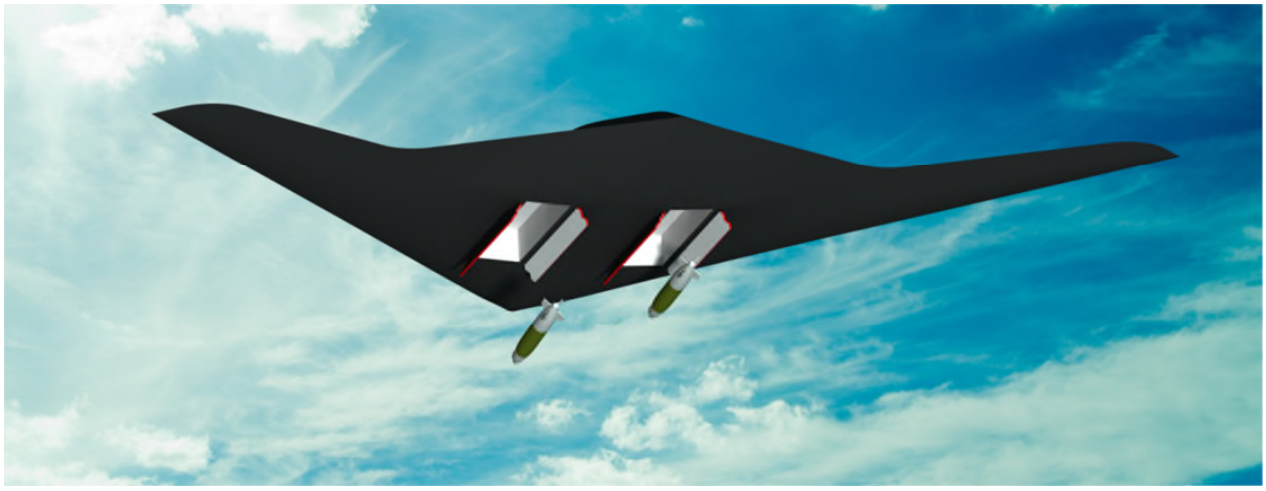

Figure 1. UCAV1303/M219-Mod000 configuration layout.

It has been designed trying to blend RCS reduction and endurance performances deriving a blended-wing-body, w-shaped layout, with a leading edge sweep of 47 degrees. Instead of mounting a single weapon bay in the belly, it is configured with two separate bays on opposite sides. Since this UCAV model has been specifically designed for CFD and wind-tunnel testing air intakes and engine exhaust have been removed from the geometry in order to make it simpler. The M219 weapon bay is a rectangular cavity with L/D ratio of 5 and W/D ratio of 1 and has been extensively used as standard bench test for analyses on transonic cavity flows. However its installation on the airframe of the UCAV1303 requires some geometry modifications. The belly of the aircraft is not flat but has a mean slope of 3.6 degrees. Moreover to safely accommodate a 500 lbs class bomb it has also been necessary to slightly stretch the cavity in transverse and longitudinal dimensions. A variant of the standard M219 cavity geometry called M219-Mod000, which details are resumed in Table 1, has been introduced. The derived cavity, compared to the M219 model, is slightly longer and wider. Leading and trailing edges are no more horizontal but inherited the outward sloping of the airframe belly implying the right side edge is at a different quote respect to the left side edge. Finally cavity floor remained unchanged and flat. The bay is accompanied by two doors with leading and trailing edges profiles double-saw-toothed at an angle of 45 degrees for RCS reduction requirements, fixed in this study to an open position of 90 degrees. The CFD model used in this study has been further simplified In fact in order to reduce the computational cost the airframe will mount only the right bay. The reference axis system (right-handed) used, with its origin at the cavity UCAV nose at the symmetry plane, is positive oriented with the X-axis

downstream and the Z-axis pointing. The far-field used for computation, with the form of an ellipsoid, centred at the origin, has the semi-axis in the X/Y/Z directions respectively of 25L, 10L and 10L. These dimension have been taken from other similar studies [11] hence, having already been proven their validity, no sensitivity study has been conducted.

Table 1. M219-Mod000 cavity geometry parameters.

DATA	VALUE	UNITS
Cavity Length (L)	2830	[mm]
Cavity Depth (D)	500	[mm]
Cavity Width (W)	700	[mm]
Cavity W/D Ratio	1.4	-
Cavity L/D Ratio	5.66	-

From the basic geometry two additional configurations where developed and tested, called respectively Mod001 and Mod002. Mod001 incorporates the installation of a saw-tooth pattern step in the cavity leading and trailing edge. This new feature was developed to permit the accommodation of the bay doors in closed position. The step height was arbitrary posed equal to 55 mm. Mod002 is a direct derivation of Mod001. In this case however the entire front and rear wall of the cavity have a saw-tooth profile instead of only a small step. The geometrical differences between the three different configurations are evidenced in Figure 2. In all three cases the geometry mounted the same bay doors ad 90 degrees opening angle.

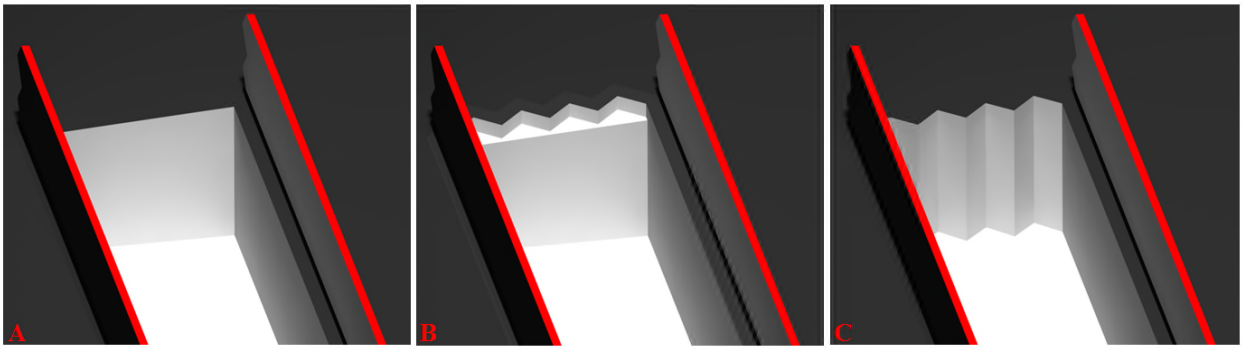

Figure 2.Views of the leading edge of the three different models. *Mod000 is the sub-figure labelled A, Mod001 the one labelled B, and Mod002 the one labelled C.*

For post-processing procedures a total of 66 probes, capable of monitoring pressure and velocity components were placed in the cavity. They were divided in 6 longitudinal rakes described in Table 2 (Note: x/L equal to 1 indicates cavity rear face, 2y/W equal to 1 indicates the side wall towards the aircraft right wingtip and z/D equal to 1 indicates cavity floor). All data has been sampled at a frequency of 10 KHz.

Table 2. Rakes coordinate for CFD analyses.

NAME	x [mm]	y [mm]	z [mm]	x/L	2y/W	z/D
Bay Origin	3450.0	1150.0	-350.0	0.0	0.0	0.0
Rake 1L	3450.0 3733.0	800.0	150.0	0.0 0.1	-0.5	1.0
Rake 1C	4016.0 4299.0	1150.0		0.2 0.3	0.0	
Rake 1R	4582.0	1500.0		0.4	0.5	
Rake 0L	4865.0 5148.0	800.0	-350.0	0.5 0.6	-0.5	0.0
Rake 0C	5431.0 5714.0	1150.0		0.7 0.8	0.0	
Rake 0R	5997.0 6280.0	1500.0		0.9 1.0	0.5	

B. Computational Methods

Detached eddy simulation is a turbulence model that blends RANS (Reynolds Averaged Navier-Stokes) modelling and LES (Large Eddy Simulation) modelling in an automatic way. The boundary, or grey area as defined in Spalart [20], between the two formulations, in many cases is not well defined and it is strongly dependant on the quality of

the mesh. There is not a practical limit to the fineness of the computational grid since finer the mesh smaller the size of eddies that are resolved instead of being modelled. A true grid convergence is never obtained since the finer the grid, the more scales are resolved and the more the simulation approaches the limit of LES with all its CPU requirements. Hence the decision of what part of the flow turbulence resolve and model is left to the user by the fact that DES adapts itself to the mesh given. Regarding the cavity flow problem the aim is to have DES modelling in the whole shear layer in order to accurately resolve the eddies responsible of the aero-acoustics. However, as shown in Thangamani et al. [21], it is of paramount importance the correct estimation of the boundary layer status at the leading-edge of the bay. So its history, i.e. the travel length before the bay edge, has to be adequately meshed in order for the RANS model to accurately resolve it. Due to the complex geometry of the problem it has been decided to use an unstructured tetrahedral type mesh with a prism layer wrapping the viscous surfaces for accurately boundary layer resolution. The critic area that had to be modelled, and hence meshed, in a proper way was identified in the shear layer, detaching from the cavity leading edge, and the flow inside the bay. For an accurate shear layer modelling with DES, Menter [22] suggests to use as mesh spacing 1/5 of the local layer thickness, being 1/20 the optimal value. In this study the 1/15 value adopted has been considered a good compromise between computational cost and quality of result. Outside the shear layer the elements have been let grown with a ratio not exceeding 1.2, i.e. dimensional difference between two adjacent elements not greater than 20%. Regarding the areas in which only RANS modelling is desired (i.e. in proximity of the aircraft surface), for an accurate resolution, Menter [22] indicates that the wall parallel and transverse spacing should be no more than the local boundary layer thickness, preferably of the order of the inertial sub layer scale. For prism layer, enveloping all viscous surfaces, Spalart [20] suggests to use an expansion ratio of 1.3 starting from a y^+ value of 0.5, as indicated in Wilcox [23] too, and to interrupt the layer growth when reaching a vertical dimension equal to half value of local boundary layer thickness. Following these indications for each case was constructed a mesh of approximately 24e+6 elements, of which 10e+6 inside the cavity. Viscous surfaces where enveloped with variable-height prims layers, composed by a total of 29 levels. The simulations were performed choosing an environmental situation representing a typical combat situation, which is a cruise Mach number of 0.85 and an altitude of 30000 ft @ ISA (International Standard Atmosphere). All other settings are listed in Table 3. The turbulent kinetic energy was estimated with the general formula:

$$k_\infty = 1.5\left(U_\infty \cdot \frac{I}{100}\right)^2 \quad \textbf{(1)}$$

Here I is the turbulence intensity (in percent). A value of 3% has been used in order to ensure the proper development of turbulent structures. Specific dissipation rate, instead, has been calculated with the following formula:

$$\omega_\infty = \frac{0.09^{0.75} \cdot k^{1.5}}{l_{ref} \cdot k} \quad \textbf{(2)}$$

Here l_{ref} has been posed equal to 0.1415 m. Eq. (1) and Eq. (2) are general formula for estimation of turbulent quantities in CFD computations involving free-airstream objects [24].

Table 3. CFD simulations reference environmental conditions.

QUANTITY	VALUE
H	30000
M_∞	0.85
U_∞	257.7
α	0.0
β	0.0
ρ_∞	0.459
p_∞	30147
T_∞	228.77
ν_∞	3.241e-05
μ_∞	1.488e-05
a_∞	303.18
k_∞	90.0
ω_∞	12.0

The unsteady simulations have been performed using the IDDES – kω SST turbulence model [25]. The air has been treated as an ideal compressible gas using Sutherland's law for viscosity modelling. Non-viscous fluxes have been resolved using 3rd order schemes, viscous ones with a 2nd order, while gradients have been evaluated using the least square method. The time marching scheme was an implicit second order dual type with 5 inner sub-iterations. The

choice of the time step has been done in order to ensure a CFL number, Eq. (3), around unity in all the elements [22].

$$CFL = \frac{dt \cdot U_{ref}}{dx} \quad \textbf{(3)}$$

Posing free-stream velocity as U_{ref} and placing dx as the minimum mesh spacing encountered in grid requirements, i.e. the spacing of the shear layer at the cavity leading edge, a dt value equal to 1.0×10^{-5} s was adopted. During the simulations has been performed a constant check to ensure that in relevant areas of the flow the CFL condition was never violated. The unsteady simulations were started from a partially converged RANS one to reduce the start-up time [22]. Finally to accurately resolve all the main modes expected in the problems the requirement of simulation duration of at least 30 cycles [22] of the frequencies of interest has been observed. In this case the aim was to resolve the physical problem up to the lowest Rossiter-Heller mode, estimated to be equal to 23 Hz [3], and hence the minimum total simulations duration requirement was 1.3 s. All the simulations where run for 140000 iterations, or 1.4 s, discarding the first 0.1 s to clean the solution from the unphysical start-up transient.

To validate the computational procedures it was performed a test run on a scaled, by a factor of 1:10.8, UCAV1303 model with the cavity installed, in order to compare the results directly with the wind tunnel data available in literature [9] for such configuration. The OASPL prediction error was confined in a band of ±4 dB. Regarding the spectral analysis the accuracy of the determination of the peak values of the modes was within ±4 dB respect to experimental data, while the location of the peaks in the frequency plane was predicted within a 20% error for the 1st mode, 15% for the 2nd mode, and 12% for the 3rd mode. The fact that with increasing frequency the error showed a decrease was correlated to the length of the sample examined. In fact while for the CFD run only 0.2 s of simulations were available, for the experimental data taken from literature a time series of 3.5 s was available. Nevertheless the precision obtained was considered satisfactory for the aim of the current study, which was based in the determination of geometrical configuration changes effects using wavelet analysis.

III. Data Analysis Procedures

Two different techniques where used to analyse the recorded signals. The standard frequency domain analysis, based on Fourier transform, and the time-frequency domain analysis based on wavelet transform.

Given a general time-series quantity $x(t)$, its frequency domain spectrum was obtained dividing the series into shorter overlapping segments, and then applying the FFT transform using a Hanning window with 90% overlap. Knowing that the Fourier transform is defined as:

$$X(\omega) = \int_{-\infty}^{+\infty} x(t) e^{-i\omega t} dt \quad \textbf{(4)}$$

The one-sided power spectral density is obtained with the following equation:

$$PSD_x = \frac{2|X(\omega)|^2}{T} \quad \textbf{(5)}$$

Where T is the temporal duration of the signal.

The Fourier analysis was accompanied by the wavelet analysis of the signal. By definition, a wavelet is a function, real or complex, $\psi(\eta)$ with a zero mean value which has to satisfy the following requirements:

$$\int_{-\infty}^{+\infty} \psi(\eta) d\eta = 0 \quad \textbf{(6)}$$

$$\int_{-\infty}^{+\infty} |\psi(\eta)|^2 d\eta = 1 \quad \textbf{(7)}$$

$$\int_{-\infty}^{+\infty} |\psi(\eta)| \, d\eta < \infty \quad \textbf{(8)}$$

$$\int_{-\infty}^{+\infty} |\psi(\eta)|^2 d\eta < \infty \quad \textbf{(9)}$$

Every wavelet can generate a family of wavelets, simply effectuating translation and dilatation in time. Given a *"Mother wavelet"* $\psi_0(\eta)$ the correspondent family is defined as:

$$\psi_{a,\tau}(\eta) = \psi_0\left(\frac{\eta - \tau}{a}\right) \quad \textbf{(10)}$$

Here $a \in R^+$is the dilatation parameter (or scale) and $\tau \in R$ is the translation parameter or localised time index. At this point, it is possible to define the *wavelet transform* of a function $x(t)$, sampled at a time step dt, as [26,27]:

$$W_x(a,\tau) = \frac{1}{\sqrt{a}} \cdot \int_{-\infty}^{+\infty} x(t) \cdot \psi^*\left(\frac{t - \tau}{a}\right) dt \quad \textbf{(11)}$$

Here the asterisk symbol indicates the complex conjugate operator. In this study, a *"Morlet"* wavelet-type has been used:

$$\psi_0(\eta) = \pi^{-1/4} \cdot e^{i\omega_0\eta} \cdot e^{-\eta/2} \quad \textbf{(12)}$$

Here ω_0 , is the *"central frequency"* of the wavelet, posed equal to 10. The scales a, of the Morlet wavelet transform, are correlated with the frequencies in which the signal is decomposed by the following equation:

$$1/f = \frac{4\pi}{\omega_0 + \sqrt{2 + \omega_0^2}} \cdot a \quad \textbf{(13)}$$

Here again, ω_0 is the central frequency defined in Eq. (12). For this study have been used a total of 256 scales spaced exponentially with base 2. Also the scales have been chosen in way to have the minimum frequency equal to the inverse of the total time duration of the signal and the maximum frequency equal to $F_s/2$. The wavelet power density (PW) can be defined as:

$$PW(a,\tau) = |W_x(a,\tau)|^2 \quad \textbf{(14)}$$

Equation (14) expresses the local wavelet power density in the time-frequency plane. The time-averaged wavelet power spectral density (PSD_ω), that can be interpreted as a smoothed version of the Fourier spectrum, is defined as:

$$PSD_\omega(a) = \frac{1}{T}\int_0^T |W_x(a,\tau)|^2 d\tau \quad \textbf{(15)}$$

Where T is the signal length. Of particular interest in the analysis of non-linear signals are the second order wavelet spectral moments [30,31]. Given a signal $x(t)$ and a couple of frequencies f_1 and f_2 along a time interval, bounded by t_0 and t_1, the wavelet auto bi-coherence (WABC) and the wavelet auto bi-spectrum (WABS) are defined as:

$$WABC_x(f_1,f_2) = \frac{|WABS_x(f_1,f_2)|^2}{\left(\int_{t_0}^{t_1}|W_x(f_1,\tau)\cdot W_x(f_2,\tau)|^2 d\tau\right)\cdot\left(\int_{t_0}^{t_1}|W_x(f_1+f_2,\tau)|^2 d\tau\right)} \quad \textbf{(16)}$$

$$WABS_x(f_1,f_2) = \int_{t_0}^{t_1} W_x(f_1,\tau)\cdot W_x(f_2,\tau)\cdot W_x^*(f_1+f_2,\tau)d\tau \quad \textbf{(17)}$$

Here $W_x(f_1,\tau)$ and $W_x(f_2,\tau)$ are the wavelet coefficients respectively at f_1 and f_2. Instead $W_x(f_1+f_2,\tau)$ are the wavelet coefficients corresponding to a frequency which is the sum of f_1 and f_2. Finally the asterisk denotes the complex conjugate. The bi-coherence is and indicator of phase coupling between the triad of waves f_1, f_2 and $f_1 + f_2$. A phase coupling between three waves implies that, naming α the phase angle of the waves, the following relation holds for the time interval under exam:

$$\alpha_{1+2} - (\alpha_1 + \alpha_2) = \xi \quad \textbf{(18)}$$

Here ξ is a constant value. If there is full phase coupling ξ will be equal to 0. So the bi-coherence function spans from 0 to 1. A value of 0 means that there is no coupling between the signal frequencies f_1 and f_2. A value greater than 0 instead represents the relative fraction that the phase of the wave $f_1 + f_2$ is due to quadratic interaction between waves at f_1 and f_2. Unlike the bi-coherence, that reveals the level of non-linearity in the system of waves, the bi-spectrum is sensitive to the magnitude of the frequency component involved in the interaction and hence can have great values, when the modules of the composing frequencies are elevated, even if the bi-coherence value is low. Hence bi-spectrum is useful in seeking eventual energy transfer between frequency components. Usually large bi-spectrum value indicates energy transfer due to quadratic interaction, even if the phase coupling is weak. Conversely a high value of phase coupling may not imply an effective energy transfer simply because none of the components in that interval contains much energy. So a threshold value must be defined. Usually only combinations of bi-coherence values greater than 0.5 and large values of bi-spectrum (usually relative levels above 0.5 calculated dividing the local WBS value by the maximum WBS value obtained in the time interval under analysis) will be considered as candidates for waves energy transfer due to non-linear phase coupling. In the overall procedure of WBS/WBC calculation, results are strongly dependant on the choice of the time interval. A too wide or too small temporal window will cause the loss or the alteration of the information contained in the signal. As a rule of thumb if f_I is the minimum frequency that is important to analyse the time interval should be at least long $2/f_I$ to ensure that at least one cycle of oscillation is processed.

When post-processing pressure signals, it is useful to define the Sound Pressure Levels (SPL) and the Overall Sound Pressure Level (OASPL) calculated using Eq. (19) and Eq. (20) . These quantities are all expressed in decibel units.

$$SPL = 10\,log_{10}\left(\frac{PSD_{p_f}(f)\cdot\Delta f_{ref}}{p^2_{reference}}\right) \quad \textbf{(19)}$$

$$OASPL = 20\,log_{10}\left(\frac{\sigma_p}{p_{reference}}\right) \quad \textbf{(20)}$$

Here $p_{refrence}$ is the minimum audible pressure, equal to 2x10^{-5} Pa, and Δf_{ref} is a reference frequency posed equal to 1Hz.

IV. Results

All numerical simulations, once discarded the non-physical start-up transient, were composed by time-histories of length 1.3 s, or 13001 samples with F_s equal to 10 KHz. Using a F_r value of 2 Hz[5], it was obtained an interval of confidence, on PSD, spanning from -2.7 dB to +4.2 dB relative to the calculated value [32]. For the determination of the confidence contours on the wavelet maps instead, it was used the technique of assuming a red-noise background spectrum obtained with the lag-1 autocorrelation coefficient [33,29]. Finally the percent error on mean quantities was estimated to be always lower than 0.5. In all the above mentioned methods it was used a 95% confidence level. In the analysis of the results it was used the approach of triple decomposition [33] to divide the flow in a time-mean part (mean flow analysis), and unsteady part (non-stationary flow analysis) where the nature of the problem was further divided in the coherent part (the Rossiter-Heller modes) and in the incoherent part (broadband noise due to general turbulence).

A. Mean Flow

The mean flow analysis was divided in the calculation of the OASPL and mean pressure coefficient in the cavity floor, and in the analysis of the mean velocity field in the cavity symmetry plane. This was considered sufficient to give an adequate picture of the time-averaged structures present in the cavity,

Figure 3 compares the OASPL values for all three geometry. It was found that the values, in each configuration, were practically symmetrical for the entire cavity's length, with a difference between the rakes that never exceeded half decibel. The reference configuration (Mod000) plot starts from 156 dB at the cavity front wall, and then immediately decreases reaching an absolute minimum of 153dB around x/L 0.2. The quantity then rises reaching a plateau, at x/l 0.5, of 160 dB, that is maintained up to x/L 0.7 where there is another positive gradient which terminates at the cavity rear wall where the maximum value of 168 dB is reached. Mod001 and Mod002 showed identical qualitative trends up to x/L 0.9. However in all the rakes the values obtained in the modified geometries were found to be 1dB below the ones of reference geometry. The exception to this was the station at x/L 0.3, in which the trend was inverted and the OASPL value in both cases was 1 dB higher than the reference. Additionally from x/L 0.6 to x/L 0.9, even if the downward shift of the curves was maintained, the offset value was found to be reduced to half decibel. The station at the rear wall of the cavity was the only one where the behaviour of Mod001 and Mod002 differed completely. While the formed maintained the half decibel shift from Mod000, the latter showed to attain itself at a lower value, 165 dB.

A similar situation was maintained for the mean pressure coefficient. In all three cases it was recorded minimal deviation spanning the cavity width, with the maximum difference always below 0.05. From the analysis of Figure 4 it is possible to see how the form of the plot assumed was the one typical of that of a transitional type cavity flow, with a quite shallow negative gradient in the first 40% of the cavity followed by sudden rise up towards positive values near the rear wall, where a maximum value of 0.2 was reached. The effects of geometry modification were negligible and even less pronounced respect to the OASPL plots. The only exception were the central and right rakes, where from x/L 0.6 to x/L 0.9, both Mod001 and Mod002 showed values 0.02 higher than the reference geometry.

The final analysis of the mean flow characteristics was conducted on the velocity vector field at the cavity symmetry plane. While this was not completely comprehensive of the full structure inside the bay, it was sufficient to understand the main features that characterised the fluid motion.

In all three configurations it was possible to recognise three distinct vortices that characterised the mean flow (indicated by points 1, 2, and 3 in each of the sub-plots of Figure 5). The main structure was formed by a big clock-wise vortex (point 2). This was responsible for the entrainment inside the cavity of the shear layer, detached from the bay leading-edge, pushing it towards the rear floor of the cavity and contributing to the high acoustic loads registered in this area. The main eddy had also a squeezed configuration, more elliptical rather than circular, probably caused by the interaction with the high speed flow just outside the cavity. The induced flow generated by this main structure in the front part of the cavity, characterised by a low-speed re-circulatory region, was the cause of the presence, in this area of the front vortex (point 1). This structure seemed to be generated by the impingement, with the front cavity's wall, of a back-ward induced stream of flow. It was possible to observe how after the

[5] Since various authors have used F_r equal to 20 Hz [9] to analyse models of 1/10 the scale the actual used model, it was decided, for this study, to use a resolution of 2 Hz.

impingement point, which constitute a saddle point in the vector field, part of the flow was re-entrained in the shear layer, while the other part was pushed downward to fed the front vortex structure.

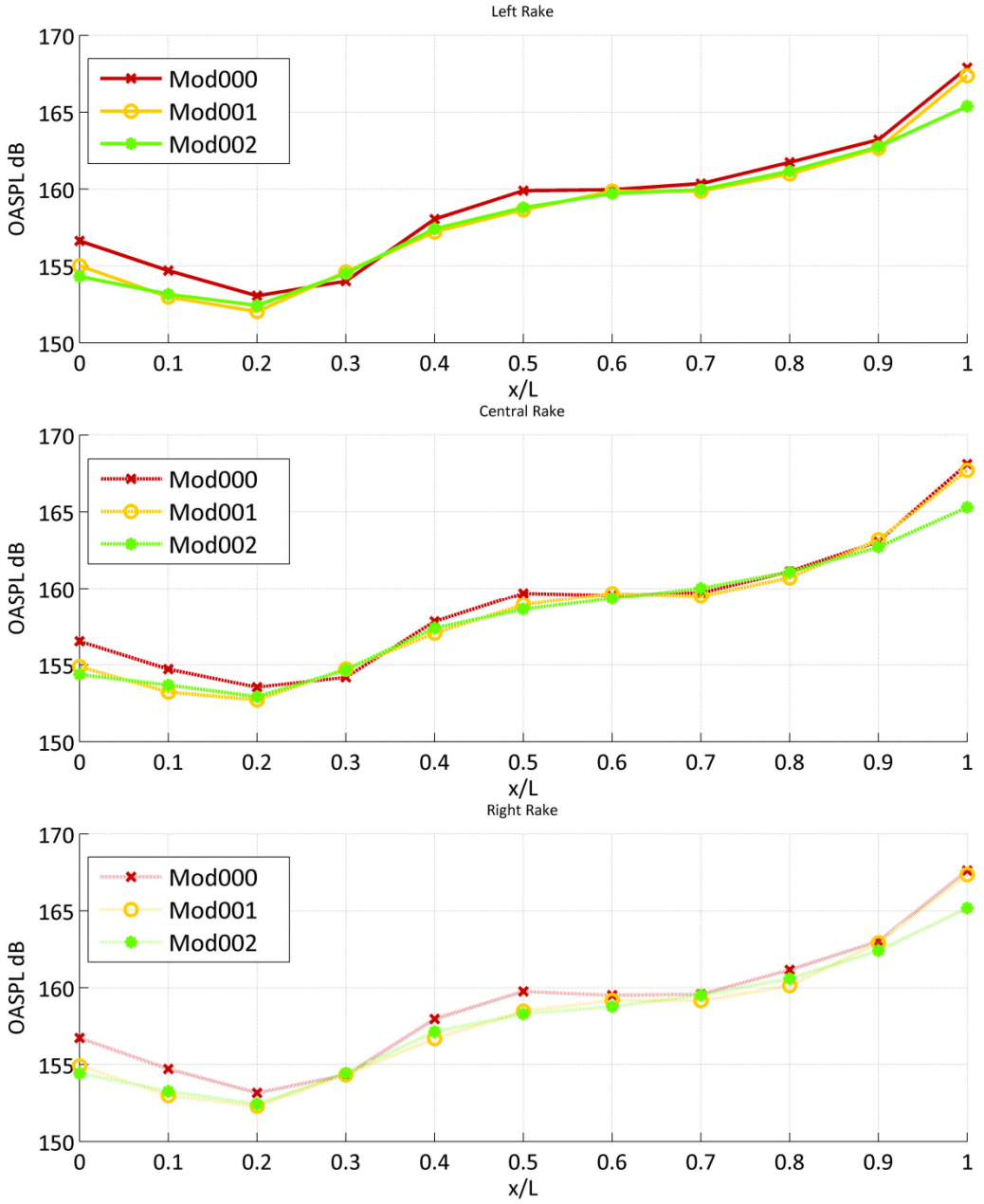

Figure 3. OASPL comparison. The plot compares the three geometrical configurations at all the rakes located on cavity's floor.

The rear vortex (point 3), with a clockwise sense of rotation, was originated by the impingement of the shear layer to a position below the bay trailing edge. The main vortex in fact (point 2) had not sufficient dimensions to sustain the bridging of the detached layer from the leading to the trailing edge. Instead in the last 30% of cavity's length the flow inside the cavity experienced a pronounced downward movement altering its almost horizontal trajectory. The consequence was a pronounced downward velocity at the rear wall that with the combined effect of the main vortex formed the eddy's structure. This was also the reason of the classification of the flow as transitional type one. The registered downward bending of the shear layer in the cavity last part is in fact the prelude to the passage from the closed cavity flow type to the open cavity flow type, where the detached layer continually increase its bend towards the bay floor up to the point it is capable to reattach itself.

Finally it was interesting to note that the minimum value of the OASPL and C_p plots was reached exactly in correspondence of the vector lines' saddle point created by the impact of the forward induced velocity of vortex 1 with the backward induced velocity of vortex 2.

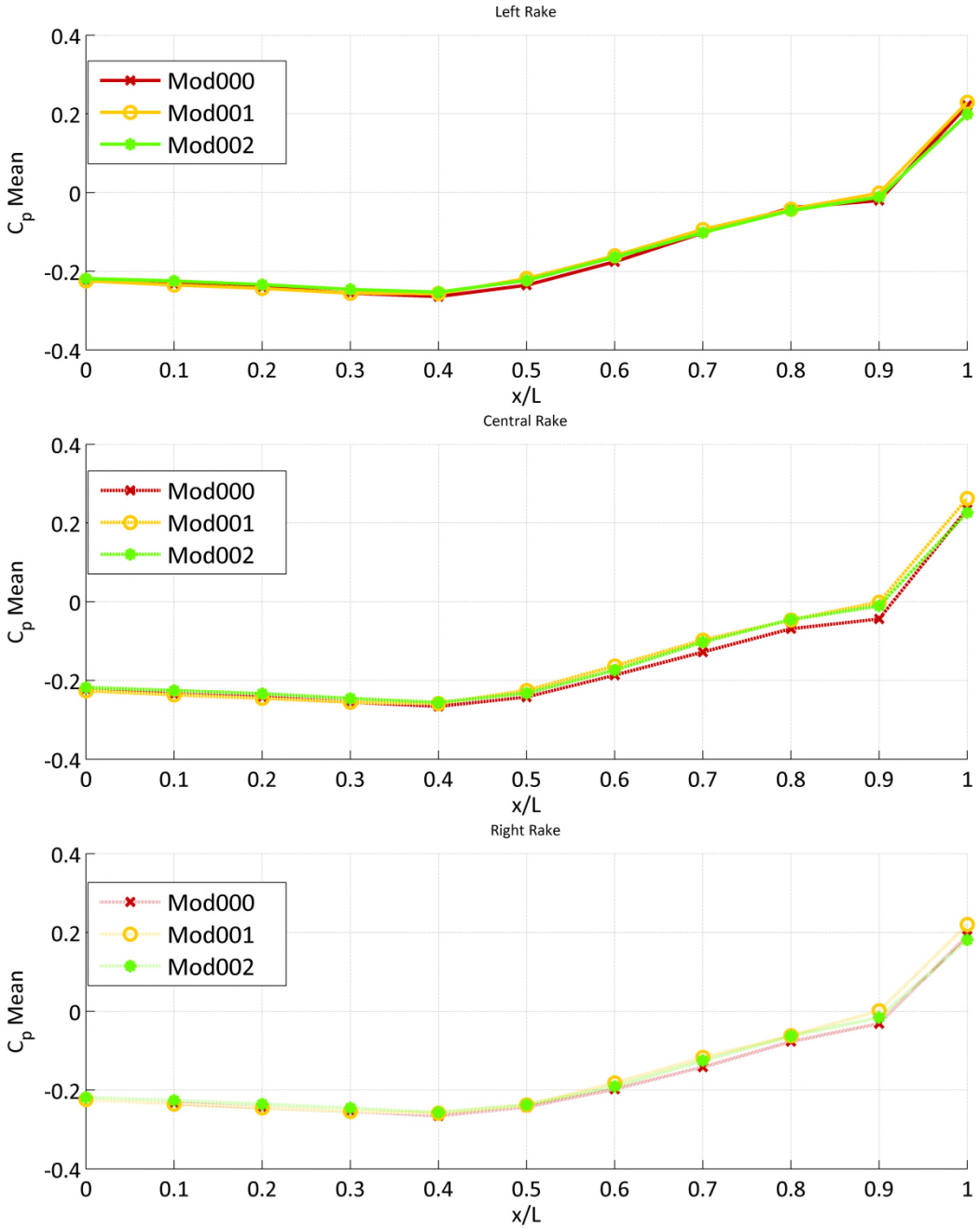

Figure 4. Mean Cp comparison. The plot compares the three geometrical configurations at all the rakes located on cavity's floor.

The effect of geometry modifications in this case differed for each vortex. The main eddy (vortex 2) was in fact displaced upwards and backwards in both Mod001 and Mod002. In either case however the overall dimensions and shape remained unchanged. Vortex 1 instead was unaffected by Mod001 but in Mod002 moved upward leading to the creation of an additive a saddle point not present in the other configurations. This particular effect could be explained by the influence in the flow patterns exercised by the saw-tooth geometry of the front wall. The effects on

vortex 3 were instead negligible on both geometry modifications implying that the rear vortex formation was only due to the relative dimensions of the main vortex respect to the cavity length and was unaffected by modifications.

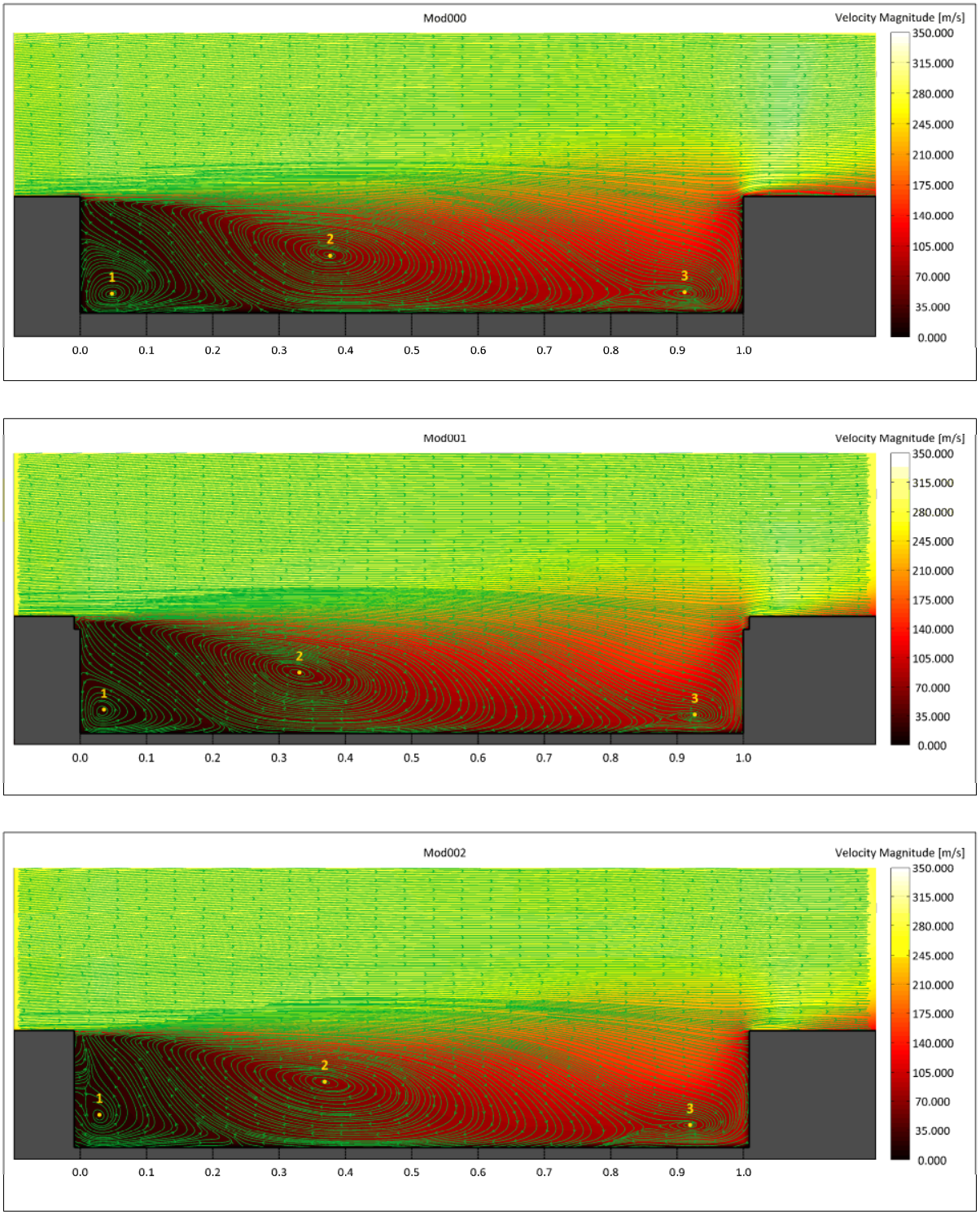

Figure 5. Mean velocity vector field at 2y/w 0.0 coloured by velocity magnitude. *Mod000 upper, Mod001 middle, Mod002 lower. The numbered points indicated the vortices centres. The impact point in the rear face of the shear layer streamlines indicates the maximum solicited area from an acoustic point of view. Flow from left to right.*

B. Non-Stationary Flow

The successive step in the analysis of the results was the conduction of the JTFA of the pressure signals. The analysis focused on the rear face of the cavity being it the most solicited area, as demonstrated by the OASPL curves. Particular attention was given to the bay's trailing-edge area due to its proximity to the impact point of the shear layer. In fact it was felt to be this location to mainly bear the unsteadiness effects and to exploit any eventual non-linear behaviour. JTFA results of all three geometry modifications are respectively shown in Figure 7, Figure 8 and Figure 9 while the tones Strouhal numbers and relative SPL levels are resumed in Table 4. All listed results refer to the analysis of the pressure signal from the probe positioned at x/L 1.0, 2y/W 0.0, and z/D 0.0.

Table 4. Spectral analysis comparison of the geometry configurations. *The table list the modes extracted from the Fourier spectrum, the wavelet time-averaged spectrum, and the Rossiter-Heller theory. Only peaks that are above the 95% power level boundary are reported. All data refers to the post-processing of pressure signal recorded at x/L 1.0, 2y/W 0.0, z/D 0.0, i.e. cavity rear face at the symmetry plane.*

Configuration	Mode ID	Fourier Spectrum		Wavelet Spectrum		Rossiter-Heller Theory	
		St	SPL dB	St	SPL_ω dB	St	SPL dB
Mod000	1st	-	-	-	-	0.255	-
	2nd	0.665	149.6	0.683	152.2		
	3rd	-	-	-	-		
	4th	-	-	-	-	0.647	
Mod001	1st	0.295	148.1	-	-		
	2nd	0.630	152.2	0.647	151.9		
	3rd	0.992	147.6	-	-	1.039	
	4th	1.381	144.6	-	-		
Mod002	1st	0.241	152.3	-	-		
	2nd	0.617	155.5	0.604	154.6	1.432	
	3rd	0.952	146.9	0.981	148.9		
	4th	-	-	-	-		

For Mod000 configuration, it was recorded both in the Fourier analysis (Figure 7-a1-2) and in the wavelet time-average analysis (Figure 7-a2-2) a main mode which corresponded to the 2nd Rossiter-Heller predicted tone. The Strouhal number was close to the theory predicted value and in both cases the deviation was below 5%. A slight difference was instead observed with the predicted power spectral density which was lower for the Fourier analysis (149.6 dB) respect to the wavelet analysis (152.2 dB). A different situation was found around the 1st Rossiter-Heller predicted tone. Alongside this Strouhal value no defined peak was found. Instead the spectrum was swallowed in a band from 0.1 St to 0.4 St (Figure 7-a1-1 and Figure 7-a2-1). Fourier PSD showed no predominance in the small peaks present in this area, while, even if wavelet PSD predicted a small dominant tone located at St 0.35, this value failed to cross the confidence level boundary preventing to assume it as a true present mode. The odd nature developed in this part of the spectrum could be explained by an analysis of the wavelet power density map (Figure 7-b). Here it was possible to see how in the band 0.1-0.4 St only mild burst of energy, widely spaced in time, were present (Figure 7-b-1). This particular aspect evidenced that the fact that, what it could be called M1, was active only in reduced time intervals, making the signal too weak to produce a tone at this Strouhal number. Moreover the location of these burst areas was also spread in a wide band along the frequency domain leading to the conclusion that M1 could not be considered a real defined tone. Only M2 could be considered a true resonant frequency due to a more regular behaviour and an ample persistence along the time domain (Figure 7-b-2). However, even if present for nearly the whole length of the signal, M2 was characterised also by an intermittent signature. At higher Strouhal numbers (>0.7) the signal was characterized by random fluctuations more correlated to broadband noise rather than organized waves.

Differing from what it was found in the mean flow analysis, the situation for Mod001 was completely different respect to the reference geometry. The presence of the different leading and trailing edge geometry modified the spectra, increasing the coherence of the 1st tone and adding a 3rd and 4th modes also (Figure 8). Fourier analysis of the signal (Figure 8-a1) placed the Rossiter-Heller tones relatively close to the calculated values and this, result confirmed too by the wavelet-time averaged spectrum (Figure 8-a2). Again the most powerful mode was the 2nd one. However while the Fourier transform predicted and increase SPL value of 3 dB respect to the Mod000 one (Figure 8-a1-2), the wavelet transform indicated an unchanged situation respect to the reference geometry (Figure 8-a2-2). This fact was explained by the structure of this mode in the wavelet power density map (Figure 8-b-2). In fact here, while the activity time of M2 was reduced, its burst of energy was increased, indicating a greater intermittency respect to the reference case. These two opposite effects counterbalanced leading, from a temporal mean point of

view, to an unchanged situation in the PSD_ω between Mod001 and Mod000. The situation for the 1st tone was similar. Again it was characterised by random energy bursts distributed in time (Figure 8-b-1). However the power levels attained in the periods of activity were greater giving in the frequency domain a better defined peak. What was particularly peculiar of Mod001 wavelet analysis was found in the existence of the 3rd and 4th modes, which in the time-frequency domain was translated in a high density of energy bursts in the band between 1 St to 2 St (Figure 8-b-3 and Figure 8-b-4). This prompted the appearance of two additional modes in the PSD plot (Figure 8-a1-3 and Figure 8-a1-4). In the PSD_ω however, even if the peaks where recognizable (Figure 8-a2-3 and Figure 8-a2-4), they both were placed below the confidence level boundary. This, in accordance with the wavelet map, showed the true nature of these tones, more similar to occasional to intermittency waves rather than well organised tones. This new signal structure could be explained by the existence of a higher level of disorganized vorticity injected in the cavity by the leading edge geometry. Instead of shedding coherent transverse-axis vortices, it was recorded (see Figure 13 a relative discussion) the production of multiple smaller eddies with various angles respect to the oncoming flow. This aspect, which favoured vortex stretching, transferred energy towards the smaller scales with their associated smaller wavelengths and hence higher frequencies.

In the case of the geometrical modification Mod002 the situation was further changed. The PSD and PSD_ω plots (Figure 9-a1 and Figure 9-a2) showed the disappearance of M1. Mode 2 in fact acquired the behaviour of an almost regular tone (Figure 9-b-2), being present for almost the whole length of the signal. This increased the relative SPL value up to 155.5 dB, the maximum registered in all three cases. This was also the only case where another mode, except for the 2nd , had enough power to cross the confidence power level boundary in the wavelet time-averaged spectrum (Figure 9-a2-3) suggesting a more regular behaviour for the 3rd tone. This was confirmed by the wavelet analysis where M3 (Figure 9-b-3), even if characterized by a still elevated intermittency, increased the amount of total time in which it was active adding more energy in its associate band. The situation for the 1st tone was again unchanged, showing only occasional bursts (Figure 9-b-1).

The different nature of the three geometries, as well as the statistical non-steadiness of the phenomenon, was also evidenced using the wavelet maxima tracking technique. This procedure consists in monitoring, at each time step of the signal, the location in the frequency plane of the absolute maximum of wavelet power density.

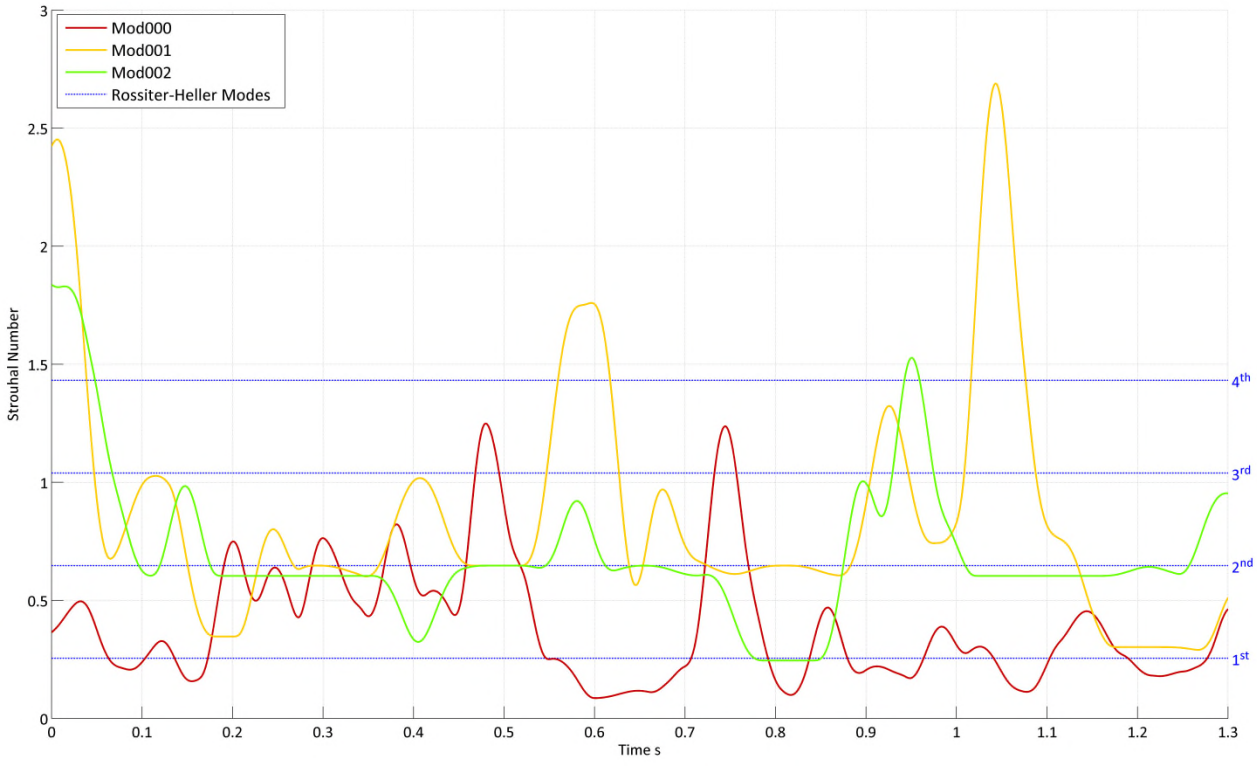

Figure 6. Dominant mode trend during time comparison. *Pressure signal at x/L 1.0, 2y/W 0.0, z/D 1.0.For each geometries the curve indicates, at each time step, at what Strouhal number is located the maximum if the wavelet power density. This enables to understand which the dominant mode is during the temporal evolution of the signal.*

The outcome is a curve plotted against time that indicated at each instant at what exact Strouhal number is located the power density maximum, or indeed which the dominant mode is at that time. This procedure was applied to all three configurations and the obtained result is plotted in Figure 6. The intermittency nature of the signal was reconfirmed for all three configurations. Along the temporal evolution it is possible to see, that even if there are time windows where attractors exist, the dominant modes oscillated continuously. Only Mod002 showed three time intervals where the dominant mode remained stable (t 0.18 s - 0.35 s and t 1.10 s – 1.19 s, where M2 was dominant, and t 0.78 s – 0.84 s, where M1 was dominant). Mod000 alternated long periods of oscillation around M2 with small passages where the maximum wandered around M1. Mod001 instead showed the most random behaviour alternating also short time intervals where the peak of energy was concentrated at high Strouhal numbers, i.e. in the broadband noise part of the spectrum.

The final step in signal post-processing was the utilisation of the WABS/WABC transforms to scan the pressure histories for any sign of non-linear interaction and phase coupling between the constituent waves. For each geometrical configuration it was decided to process an interval of 0.2 s placed at the time in which the dominant mode (M2) reached its absolute maximum wavelet power density. These were from 0.5 s to 0.7 s for Mod000, 0.7 s to 0.9 s for Mod001, and 0.5 s to 0.7 s for Mod002. The decision to adopt a 0.2 s interval was such that the duration was enough to cover at least two cycles of the minimum resolved frequency (i.e. 20 Hz that is below the 1st Rossiter-Heller value) and that was not too much longer to lose the temporal resolution. Finally, centring the interval on a maximum peak of energy gave an insight picture of the phenomenon in a worst condition case. The result of the WABS/WABC analyses is summarised, for each configuration, in Figure 10, Figure 11, and Figure 12.

The depicted maps represent all the possible interactions in the admissibility domain and show the superimposition of the contours of WBC (black to white colours) and the contours of WBS (blue colours) which identifies the threshold limits of energy transfer. Non-linear interaction, with high energy transfer, is likely to occur in areas in which both WBS and WBC values are above 0.5. Each point of the map represents the WBS/WBC value of a Strouhal number which is the result of the summation of the abscissa and the ordinate of the point. Hence, being the ordinate axis spanning from negative to positive values, both summation and difference combination of Strouhal numbers are covered. The bright-green dashed lines show the limits of the domain of computation. The map is symmetric around these lines hence the values outside this boundary are not visualised. To help the reading of the plot, bands of constant values are displayed as dash-dot dark green lines. These bands enclose all the points which sum of the abscissa and the coordinate is constant.

For Mod000 it was recorded only one triplet[6] which represented the interaction of M2 with M1 that created a sub-mode, Sb_{M2-M1} (Figure 10-1a, 1b, and 1c). The excitation of this wave explained the absence in Figure 7's spectra of a well-defined peak around the 1st theory-predicted Rossiter-Heller tone. The presence of $Sb1_{M1|M2}$ interfered with the eventual formation of M1 leading to the appearance of the 1st tone only in reduced time intervals which total duration was too small to create a strong foot-print in the Fourier and wavelet time-averaged spectra. Usually are required at least 30 cycles of a relative frequency to adequately estimate the power contained in that band. However, how can be seen from Figure 7, the particular nature of M1 was such that it was active for a cumulative time of no more than 0.5 s, leading to a total of 10 cycles, a third of the required value. An explanation on the causes of the generation of a sub-mode relies on the fact that the Rossiter-Heller modes, being not arithmetically exact harmonics, when undergo non-linear interaction, won't exchange energy between them but will create a third wave with whom form a phase-coupled system.

In Mod001configuration it was maintained the sub-mode $Sb1_{M1|M2}$ (Figure 11-1a, Fig 11-1b, and Fig 11-1c). However the WBS/WBC values were lower respect to Mod000 case, implying a lower power for the derived wave. This geometry configuration showed also a second interaction (Figure 11-2a and Fig11-2b) where M2 was able to excite its first harmonic, $H1_{M2}$. The coupling however was feeble and the effects on the spectrum were minimal. The situation was similar for Mod002. Again two derived waves were present, the sub-mode combination of M1 and M2, $Sb1_{M1|M2}$ (Figure 12-1a, Fig 12-1b, and Fig 12-1c), and the first harmonic of M2, $H1_{M2}$ (Figure 12-2a and Fig 12-2b), and again the interaction was minimal, leading to negligible effects on the spectra.

The WABS/WABC indicated that the introduction of the saw-tooth pattern in the transverse edges of the bay nearly eliminated the non-linear interaction between the 1st and 2nd tones present in the spectrum. This could be the reason behind the appearance, in the spectra of Mod001 and Mod002, of a higher and better defined peak around the 1st Rossiter-Heller theory-predicted value. This fact however was detrimental since the higher coupling between M1

[6] The WABS/WABC map indicates the combination where the interaction of a wave at frequency f_i with a wave at frequency f_j gives birth to a wave at frequency $f_k=f_i+f_j$. Hence when looking for phase couplings area, it is usually scanned for groups of three waves. The only exception is when harmonics and sub-harmonics are created. In this case couple of waves are found, i.e. $f_k=2f_i$ or $f_k=0.5f_i$.

and M2, registered in Mod000, introduced a beneficial effect where part of the energy of the two main tones was redirected towards $Sb1_{M1|M2}$ reducing the SPL values in band below 0.5 St.

The geometry modification effects on the fluid structure were also evidenced analysing the flow inside the cavity using the Q-criterion. Snapshots of iso-surfaces of Q equal to $100(L/U_\infty)^2$ were taken for all three geometries, but in each case at different times, corresponding to the absolute maximum of wavelet power spectral density, i.e. t 1.10 s for Mod000, t 0.84 s for Mod001, t 1.15 s for Mod002. In all cases the snapshots were located in a time band where the dominant mode was the second one. The comparison plot is shown in Figure 13. In the reference configuration (Mod000) it was possible to recognise the alternate detachment of transverse axis vortices at the leading edge (point 1), followed by a destabilisation and tilt (point 2) that contributed to stretch the vorticity tubes and to re-arrange their orientation and size, up to the point where, approaching the trailing edge (point 3) the original organization was completely forgotten. Here were present some very big organised structures and a lot of small blobs of vorticity, which decay is a great source of the noise [33].

When the first geometrical modification was introduced the main effect was found in the different fluid structures present at the leading edge of the cavity. The transverse lump of vorticity, that was characterizing Mod000, was replaced by different structures, independent from one another, due to the effect of the saw-tooth pattern (point 1). At each indentation it was registered the released a couple of small longitudinal-axis vortices that, respect to the reference case, produce an enhanced vortex stretching and cascade towards smaller sizes. The splitting of vorticity induced by the geometry of the leading edge prompted an immediate passage to disordered geometries which may be the cause for the slightly increase in modes power respect to the reference case. Also the presence of the saw-tooth pattern at the leading edge favoured the size-cascade mechanism and it was probably the cause of the increased intermittency of the pressure signal, respect to the straight-leading edge geometry, registered in this area. It was also observed that the fluid structures inside the cavity were less organized and had a slightly lower overall velocity respect to the reference geometry case.

In Mod002, as in the case of Mod001the axis-oriented vortices detachment was maintained (point 1) as well as the enhanced eddy-break up immediately thereafter (point 2). However in the rear of the cavity (point 3), it was registered and increased number of vortex structures that seemed to originate from the saw-toot face. This was correlated to the characteristic lower OASPL value of Mod002 respect to the other two geometries showed in Figure 3. In all other aspect the structure remained similar to the one of Mod001.

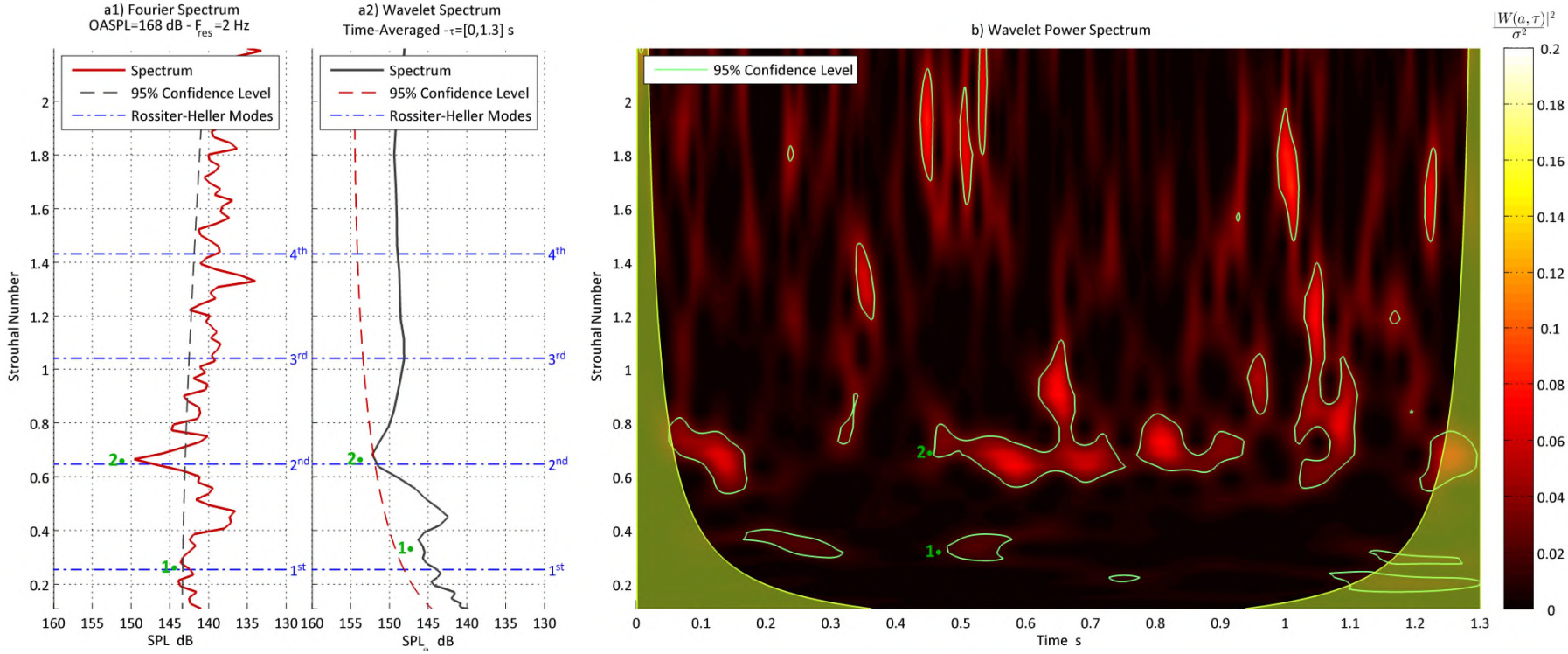

Figure 7. Wavelet and Fourier analysis of pressure signal a cavity rear face, Mod000, x/L 1.0, 2y/W 0.0, z/D 0.0. *Subplot a1 shows the Fourier analysis, subplot a2 shows the wavelet time-averaged power spectrum while subplot b is the wavelet power density map normalized by signal variance. In all cases 95% confidence power level boundaries are shown.*

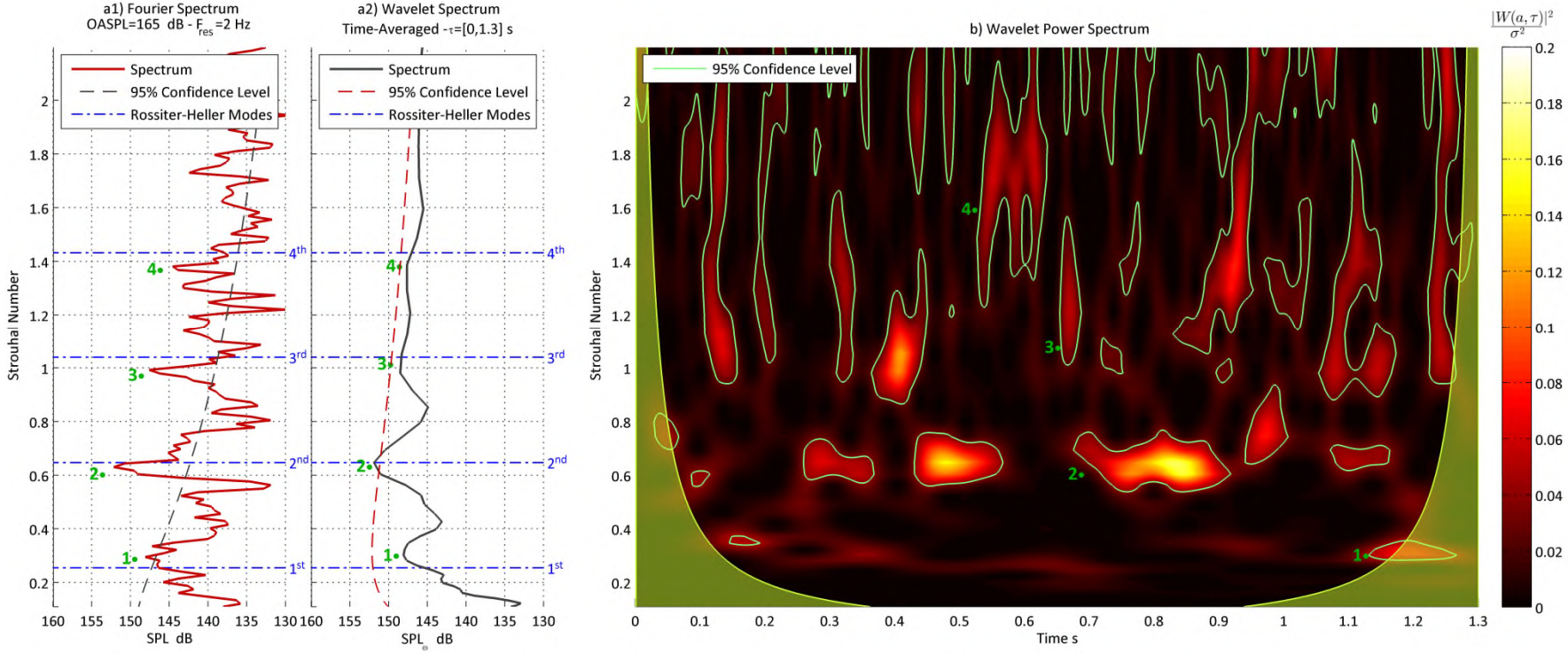

Figure 8. Wavelet and Fourier analysis of pressure signal a cavity rear face, Mod001, x/L 1.0, 2y/W 0.0, z/D 0.0. *Subplot a1 shows the Fourier analysis, subplot a2 shows the wavelet time-averaged power spectrum while subplot b is the wavelet power density map normalized by signal variance. In all cases 95% confidence power level boundaries are shown.*

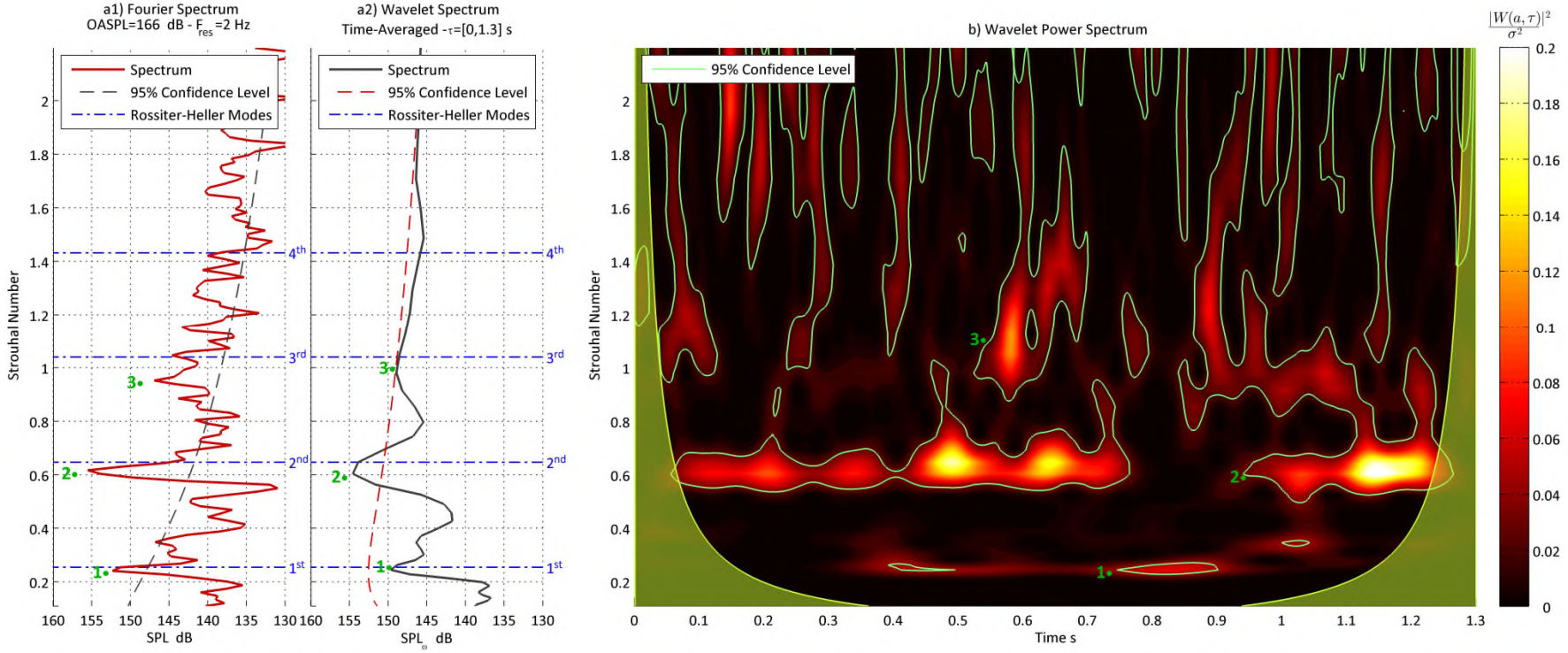

Figure 9. Wavelet and Fourier analysis of pressure signal a cavity rear face, Mod002, x/L 1.0, 2y/W 0.0, z/D 0.0. *Subplot a1 shows the Fourier analysis, subplot a2 shows the wavelet time-averaged power spectrum while subplot b is the wavelet power density map normalized by signal variance. In all cases 95% confidence power level boundaries are shown.*

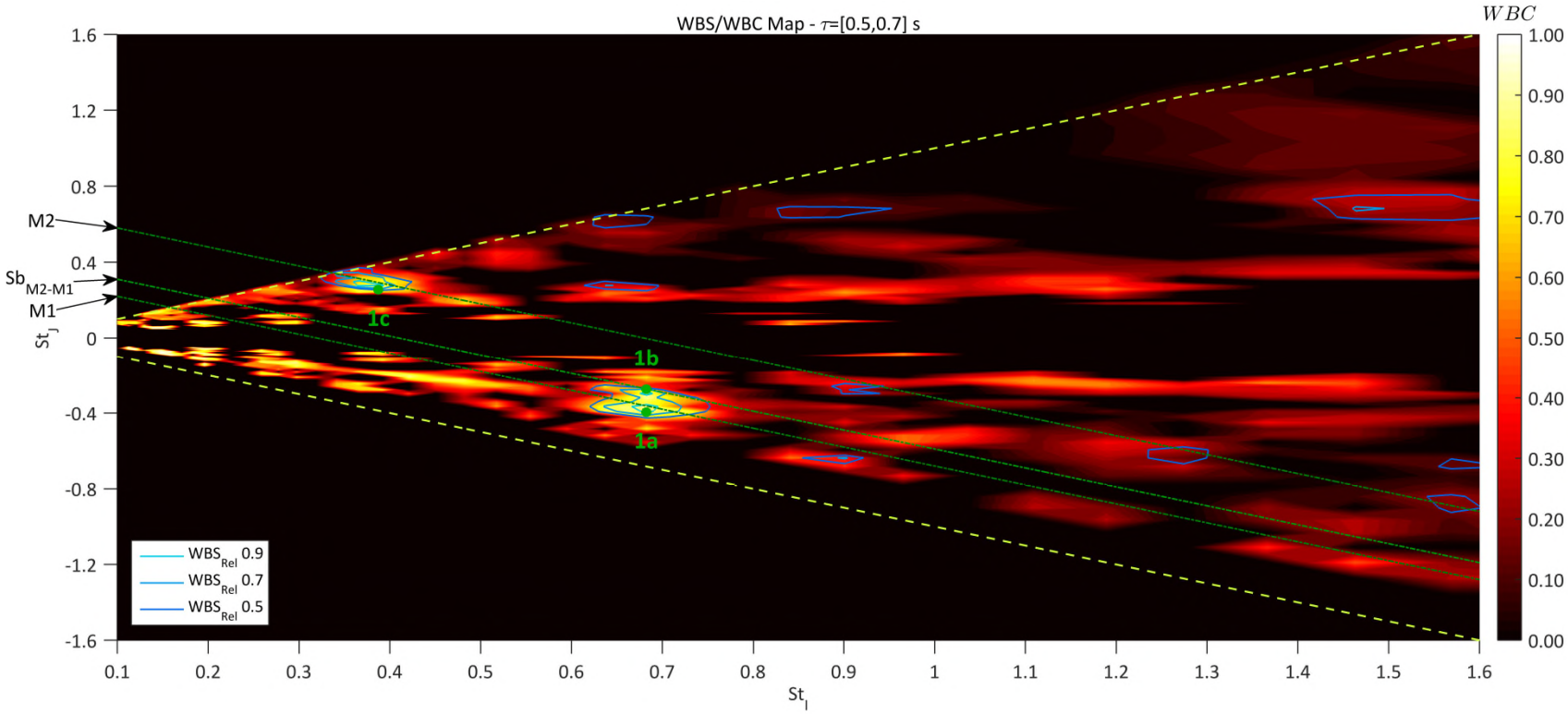

Figure 10. Wavelet auto-bi-spectrum and coherence of pressure signal a cavity rear face, Mod000, x/L 1.0, 2y/W 0.0, z/D 0.0. *The time of analysis was between 0.5 s and 0.7 s. Areas of high energy transfer are individuated by the super-imposition of WBS contours and WBC contours. Negative-constant-slope lines points which algebraic sum is constant.*

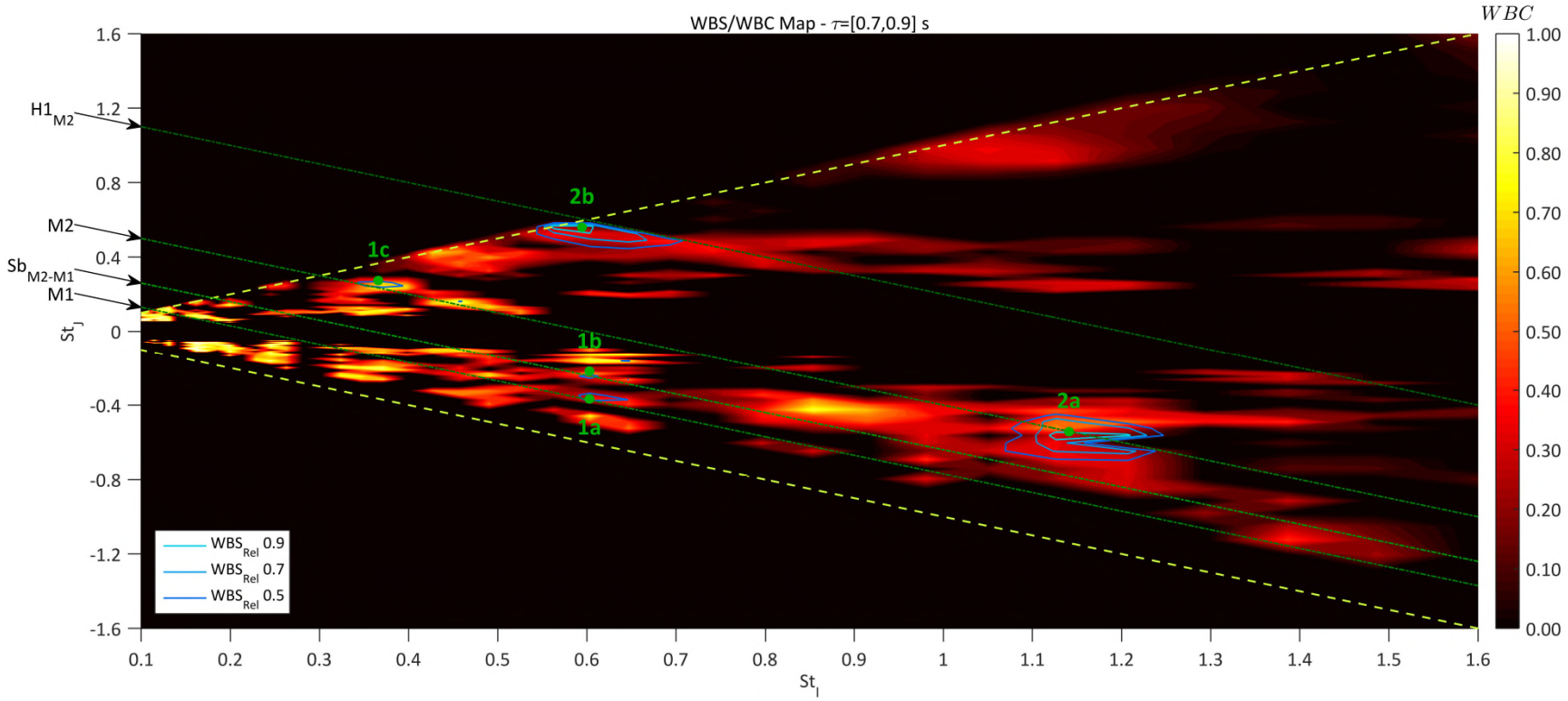

Figure 11. Wavelet auto-bi-spectrum and coherence of pressure signal a cavity rear face, Mod001, x/L 1.0, 2y/W 0.0, z/D 0.0. *The time of analysis was between 0.7 s and 0.9 s. Areas of high energy transfer are individuated by the super-imposition of WBS contours and WBC contours. Negative-constant-slope lines points which algebraic sum is constant.*

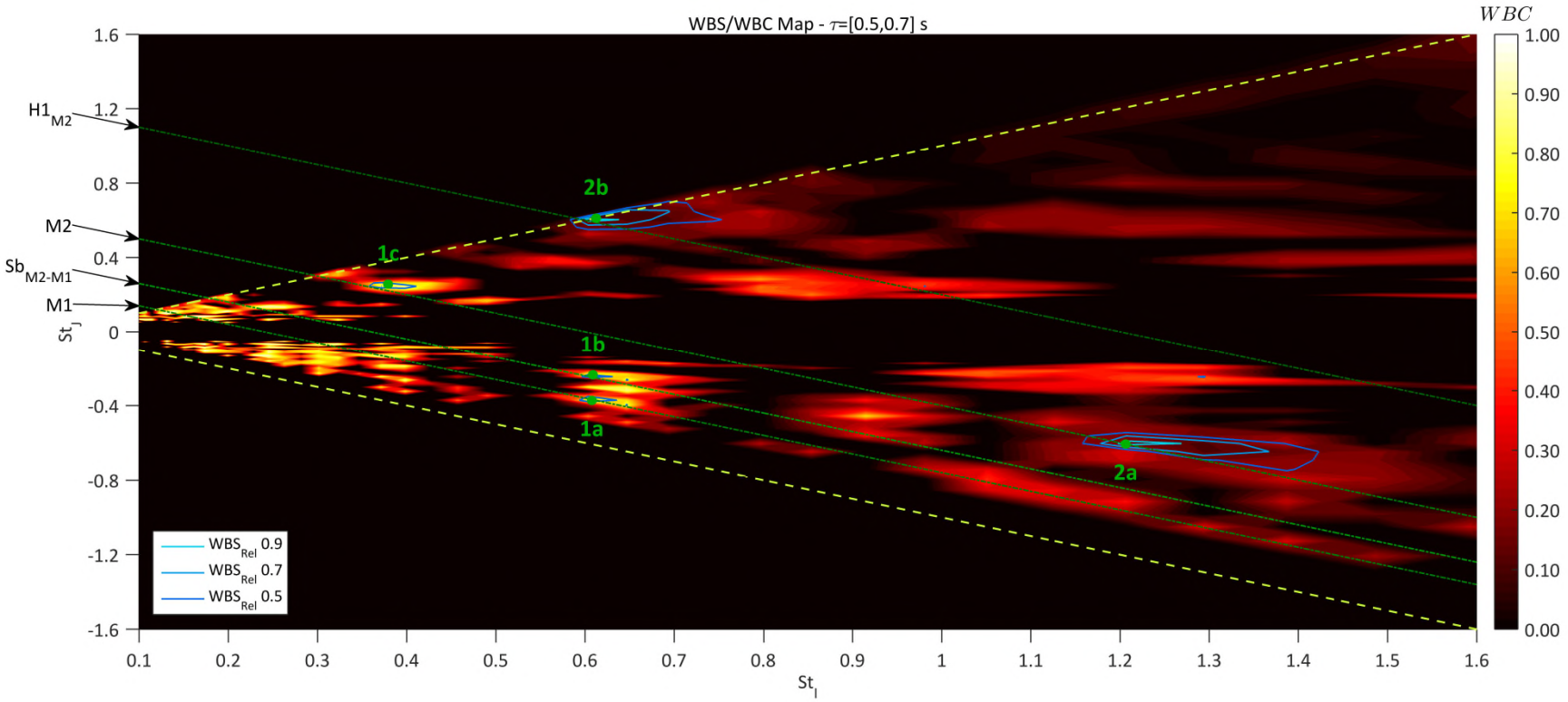

Figure 12. Wavelet auto-bi-spectrum and coherence of pressure signal a cavity rear face, Mod002, x/L 1.0, 2y/W 0.0, z/D 0.0. *The time of analysis was between 0.5 s and 0.7 s. Areas of high energy transfer are individuated by the super-imposition of WBS contours and WBC contours. Negative-constant-slope lines points which algebraic sum is constant.*

.

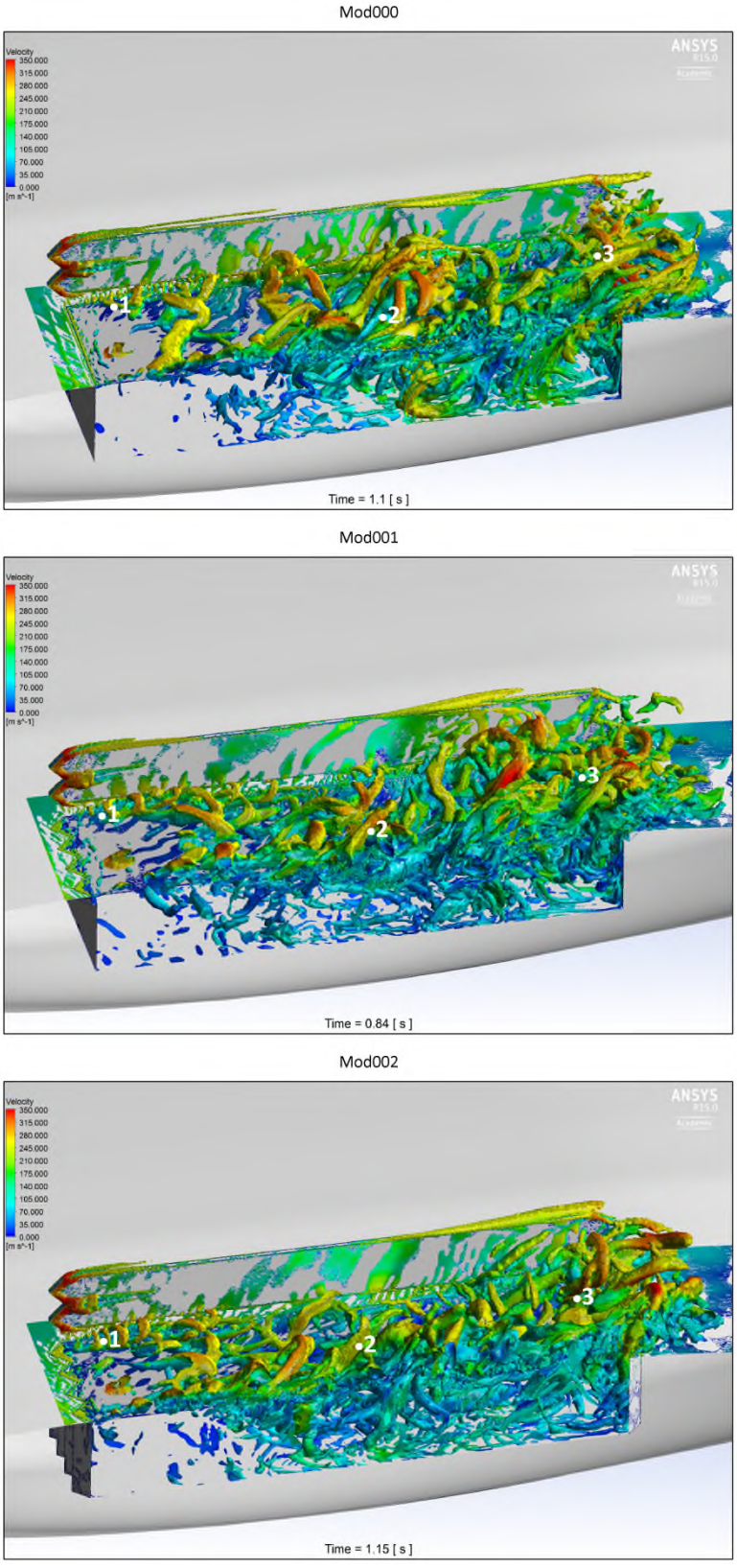

Figure 13. Iso-surface of $Q = 100 \cdot L^2/U_\infty^2$. *The pictures where taken at three different times each corresponding to the absolute maximum of the wavelet power spectral density. Flow from left to right.*

V. Conclusions

JTFA of three cavity types, deriving from the Boeing M219 model and installed in a full-scale Boeing UCAV1303, was conducted upon pressure signals registered in CFD numerical simulations. The three configurations tested were the reference one, called Mod000, with straight leading and trailing edges, Mod001 with saw-tooth pattern at the transverse edges and a step of 55 mm height, and Mod002 with the front and rear faces with a saw-tooth surfaces.

The mean flow analysis and the inspection of the velocity vector field inside the cavity revealed transitional type behaviour, with the presence of three vortices. The maximum OASPL levels were registered in the rear face, with values up to 168dB. The effect of geometrical variations was nearly absent in the mean C_p curves, while the OASPL levels, in both Mod001 and Mod002, where inferior of 1 dB in the first 20% of the cavity respect to the reference case. At the bay rear face the situation was different, in fact while Mod000 and Mod001 reached an OASPL value of 168 dB, in Mod002 it was recorded a value of 165 dB.

The non-stationary flow analysis revealed the statistical unsteadiness of the pressure signals recorded during the experiments. In all cases the most powerful tone was the 2nd Rossiter-Heller one, which was always located close to the theory predicted value (Mod000: 149.6 dB @ 0.665 St, Mod001: 152.2 dB @ 0.63 St, Mod002 155.5 @ 0.61 St). Wavelet analysis showed the intermittency nature of the phenomenon and evidenced non-linear aspects like dominant mode switching during the temporal evolution of the pressure signals. The main effects of the introduction of the saw-tooth modifications was the increasing of the intermittence and the introduction of the 3rd and 4th tone in Mod001 and the 3rd tone in Mod002.

Wavelet auto-bi-spectrum analysis of the signal showed in all cases a non-linear phase coupling between the 1st and 2nd Rossiter-Heller modes that created a third wave, located at the two tones algebraic differences, that particularly influenced the behaviour of the 1st tone, reducing its time of activity at small bursts of energy widely spread in the time domain. The introduction of the geometrical modifications slightly reduced this coupling and also prompted the creation of the 1st harmonic of the 2nd mode.

With the aid of Q-criterion visualisation technique it was possible to evidence the difference pattern of separation of the shear layer. While for the reference case it was recorded the standard alternate detachment of transverse axis vortices, the saw-tooth pattern prompted the creation of smaller vortices of nearly transverse axes. This spilt of vorticity favoured the decay of eddies to smaller scales which may be the cause for the slightly increase in modes power respect to the reference case. In the rear of the cavity of Mod002 it was registered and increased number of coherent vortex structures explaining the reduced OASPL levels respect to the other two geometries.

VI. References

1. **Rockwell, D. and Naudasher, E.** Review of Self Sustaining Oscillation of Flow Past Cavities. *Journal of Fluids Engineering.* 1978, Vol. 100, pp. 152-165.

2. **Rossiter, J.** *Wind Tunnel Experiments on the Flow Over Rectangular Cavities at Subsonic and Transonic Speeds.* s.l. : Aeronautical Research Council Reports and Memoranda. TR-3438, 1966. Technical Report 3438.

3. **Heller, H., H., Holmes, D., G. and Covert, E., E.** Flow Induced Oscillations in Shallow Cavities. *Journal of Sound and Vibration.* 1971, Vol. 18, pp. 545-553.

4. **Tracy, M., B. and Plentovich, E., B.** *Characterisation of Cavity Flow Fields Using Pressure Data Obatained in the Langley 0.3-Meter Transonic Cryogenic Tunnel.* Langley Research Center. Hampton, Virginia : s.n., 1993. NASA Technical Memorandum 4436.

5. **Ahuja, K., K. and Mendoza, J.** *Effects of Cavity Dimensions Boundary Layer and Temperature on Cavity Noise with Emphasis on Benchmark Data to Validate Computational Aeroacoustic Codes.* s.l. : NASA CR-4653, 1995.

6. *Computational Modeling of Geometrically Complex Weapon Bays.* **Kannepalli, C., et al., et al.** 2011. 17th AIAA/CEAS Aeroacoustic Conference.

7. **Ukeiley, L., Arunajatesan, S. and Jansen, B., J.** Control of Pressure Loeads in Geometrically Complex Cavities. *Journal of Aircraft.* 2008, Vol. 45, 3, pp. 1014-1024.

8. **Casper, K., M., et al., et al.** Complex Geometry Effects on Cavity Resonance. *AIAA Journal.* 2016, Vol. 54, 1, pp. 320-330.

9. *Aero-acoustic Environment Within the Weapons Bay of a Generic UCAV.* **Chaplin, R., A. and Birch, T., J.** New Orleans : s.n., 2012. 30th AIAA Applied Aerodynamics Conference. pp. 1-26. AIAA 2012-3338.

10. **Clark, R., L.** *Evaluation of F-111 Weapon Bay Aeroacoustic and Weapon Separation Improvement Techniques.* Air Force Flights Dynamic Laboratories. 1979. AFFDL-TR-79-3003.

11. **Lawson, S., J. and Barakos, G., N.** Evaluation of DES for Weapon Bays in UCAV. *Aerospace Science and Technology.* 2010, Vol. 14, pp. 397-414.

12. **Murray, N., E. and Jansen, B., J.** Effect of Door Configuration on Cavity Flow Modulation Process. *AIAA Journal.* 2012, Vol. 50, 12, pp. 2932-2937.

13. **Lawson, S.,J. and Barakos, G.** Review of Numerical Simulations of High-Speed Turbulent Cavity Flows. *Progress in Aerospace Sciences.* 2011, Vol. 47, pp. 186-216.

14. **Camussi, R., Gilles, R. and Jacob, M., C.** Cross-Wavelet Analysis of Wall Pressure Fluctuations Beneath Incompressible Turbulent Boundary Layers. *Journal of Fluid Mechanics.* 2008, 617, pp. 11-30.

15. **Li, H.** Identification of Coherent Structure in Turbulent Shear Flow with Wavelet Correlation Analysis. *Journal of Fluids Engineering.* 1998, Vol. 120, pp. 778-785.

16. **Lee, I. and Sung, H., J.** Multiple-Arrayed Pressure Measurement for Investigation of the Unsteady Flow Structure of a Reattanching Shear Layer. *Journal of Fluid Mechanics.* 2002, Vol. 463, pp. 377-402.

17. **Watanabe, T., et al., et al.** Wavelet Analysis of Coherent Vorticity near the Turbulent Non-Turbulent Interface in a Turbulent Planar Jet. *Physics of Fluids.* 2014, Vol. 26, pp. 095105(1)-095105(18).

18. *Relationship between Acoustic Tones and Flow Structure in Transonic Cavity Flow.* **Wagner, J., L., et al., et al.** Dallas : AIAA Aviation, 2015. 45th AIAA Fluid Dynamics Conference. pp. 1-16.

19. **Kegerise, M., A., et al., et al.** Mode-Switching and Nonlinear Effects in Compressible Flow over Cavity. *Physics of Fluids.* 2004, Vol. 16, 103, pp. 678-687.

20. **Spalart, P., R.** *Young Person Guide to DES Grids.* Langley Research Center. Hampton, Virginia : s.n., 2001. NASA CR-2001-211032.

21. **Thangamani, V, Knowles, K. and Saddington, A., J.** Effects of Scaling on High Subsonic Cavity Flow Oscillations and Control. *Journal of Aircraft.* 2014, Vol. 52, 2.

22. **Menter, F., R.** *Best Practice for Scale Resolving Simulations in ANSYS CFD.* s.l. : ANSYS, 2012.

23. **Wilcox, D., C.** *Turbulence Modeling for CFD, 3rd Edition.* s.l. : DCW Industries - ISBN 9781928729082, 2006.

24. **Spalart, P., R. and Rumsey, C., L.** Effective Inflow Conditions for Turbulence Models in Aerodynamic Calculations. *AIAA Journal.* 2007, Vol. 45, 10, pp. 2544-2553.

25. **Shur, M., L., et al., et al.** A Hybrid RANS-LES Approach with Delayed-DES and Wall-Modelled LES Capabilities. *International Journal of Heat and Fluid Flow.* 2008, Vol. 29, pp. 1638-1649.

26. **Grossmann, A. and Morlet, J.** Decomposition of Hardy Functions into Square Integrable Wavelets of Constant Shape. *SIAM Journal of Mathematical Analysis.* 1984, Vol. 15, 4, pp. 723-736.

27. **Daubechies, I.** *Ten Lectures on Wavelets.* Philadelphia : Philadelphia Society for Industrial and Applied Mathematichs - ISBN 0898712742, 1992.

28. **Van Milligen, B. ,P., et al., et al.** Wavelet Bicoherence : A New Turbulence Analysis Tool. *Physics of Plasmas.* 1995, Vol. 2, 8, pp. 3017-3032.

29. **Ge, Z. and Liu, P., C.** A Time-Localized Response of Wave Growth Process Under Turbulent. *Annales Geophysicae.* 2007, Vol. 25, pp. 1253-1262.

30. **Newland, D., E,.** *An Introduction to Random Vibrations, Spectral & Wavelet Analysis.* Harlow : Longman Group Limited, 1993.

31. **Torrence, C. and Compo, G., P.** A Practical Guide to Wavelet Analysis. *American Meteorogical Society.* 1998, Vol. 79, 1, pp. 61-78.

32. **Torrence, C. and Webster, P., J.** Interdecadal Changes in the ENSO-Monsoon System. *Journal of Climate.* 1999, Vol. 12, pp. 2679-2690.

33. **Hussain, A., K.** Coherent Structures and Turbulence. *Journal of Fluid Mechanics.* 1986, pp. 303-356.